Chapter 4
From Functional Architectures to Percepts: A Neuromathematical Approach

Giovanna Citti and Alessandro Sarti

Abstract. In this paper we will consider mathematical models of the functional architecture of the primary visual cortex based on Lie groups equipped with sub-Riemannian metrics. We will critically review and clarify our line of work, joining together within an integrative point of view geometric, statistical, and harmonic models. The neurogeometry of the cortex in the SE(2) groups introduced recalling the original paper [12]. Amodal perceptual completion is reconsidered in terms of constitution of minimal surfaces in the geometric space of the functional architecture, and a new Lagrangian field model is introduced to afford the problem of modal perceptual completion [14] of the Kanizsa triangle. The neurogeometric structure is considered also from the a probabilistic point of view and compared with the statistics of co-occurence of edges in natural images following [48]. Finally the problem of perceptual units constitution is introduced by means of a neurally based non linear PCA technique able to perform a spectral decomposition of the neurogeometrical operator and produce the perceptual gestalten [52, 53].

4.1 Introduction

The pioneeristic work of Hubel and Wiesel in the seventies [32, 33] allowed the discovery of the modular structure of the mammalian visual cortex. Every module is composed by many families of cells, every one sensible to a specific feature of the image, either position, orientation, scale, color, curvature, velocity or stereo. Modules are spatially arranged in suitable maps always respecting retinotopy in such a way that for every point (x,y) of the retinal plane there is a hypercolumn containing

Giovanna Citti
Dipartimento di Matematica, University of Bologna
e-mail: giovanna.citti@unibo.it

Alessandro Sarti
CAMS Center of Mathematics, CNRS-EHESS, Paris
e-mail: alessandro.sarti@ehess.fr

G. Citti and A. Sarti (eds.), *Neuromathematics of Vision,*
Lecture Notes in Morphogenesis,
DOI: 10.1007/978-3-642-34444-2_4,

an entire set of cells sensitive to all feature instances. The functional architecture of the visual cortex is the geometric machine underlying the processing of visual stimuli, and it is defined in terms of hypercolumnar organization and its neural connectivity. A particularly interesting framework to mathematically model the functional architecture of the primary visual cortex has been introduced first by W.C. Hoffmann in [30]. A differential geometry setting has been proposed to model the hypercolumnar organization in in terms of a manifold equipped with a fiber bundle structure. Steven Zucker in [61] followed a similar approach to model the action of simple cells for orientation detection, introducing Frenet frames in a fiber bundle structure to represent hypercolumns. Jean Petitot and Yannique Tondut in [46] introduced in the fiber bundle structure a supplementary constraint, giving rise to the so called contact structure. They propose for the first time the notion of neurogeometry. The contact constraint is fundamental to take into account the anysotropic pattern of connectivity between hypercolumns. Citti and Sarti proposed to represent the functional architecture in terms of Lie group structures equipped with sub-Riemannian metrics, which better describe the symmetry of the cortex [12]. In their model, the hypercolumnar structure is described in terms of the Lie symmetries of the Euclidean group, equipped with the suitable sub-Riemannian metric for modelling anysotropic connectivity. The integral curves of its generating vector fields can also be considered as a mathematical representation of the association fields of Field, Hayes and Hess [23]. The propagation in the sub-Riemannian setting allows to perform amodal contour completion [12]. With similar instruments, both contour and image completion have been achieved in the Lie group of affine transformation in [49] and improved by introducing the hyperbolic plane in [50]. Analytical properties of the model [12] was further studied by R. Hladky and Pauls [29]. Finally we recall the works of Duits, van Almsick, Franken, ter Haar Romeny [19] [20] [21] who proposed new models in different Lie groups, with many applications to image processing. The connectivity kernels resulting from the sub-Riemannian model of the cortex are compared with the statistics of co-occurence of edges in natural images in [48], giving a possible explanation of their emergence. In [14] a Lagrangian field model is introduced to couple the functional architecture of the Lateral Geniculate Nucleus with the one of the visual cortex. The resulting model is able to afford the problem of modal perceptual completion of the classical triangle of Kanizsa. The problem of the constitution of perceptual units in the geometry of the functional architecture is the very question to fill the gap between neurophysiology and phenomenology of perception. In [52] and [53] a mechanism of grouping has been proposed as extension of the model of visual hallucination proposed by Bressloff and Cowan [7]. The model performs a non-linear Principle Component Analysis by using the neurogeometrical kernels of the functional architecture.

In this paper we will critically review and clarify our line of work, joining together within an integrative point of view geometric, statistical and harmonic models previously presented. The paper is organized in six main parts. In section 4.2, the functional architecture of the Lateral Geniculate Nucleus is presented, while in section 4.3, the neurogeometry of the cortex is recalled following [12]. In section 4.5, a model of amodal perceptual completion is proposed in terms of constitution

of minimal surfaces in the geometric space of the functional architecture. In section 4.6, a Lagrangian field model is introduced to afford the problem of modal perceptual completion [14]. In section 4.7, we will reinterpret the neurogeometric structure from a probabilistic point of view and compare it with the statistics of co-occurence of edges in natural images, following [48]. In section 4.8, we will afford the problem of perceptual units constitution. By means of a sinlge neural population model [8], we will construct the gestalten performing a spectral decomposition of the neurogeometrical operator.

4.2 Functional Architecture of Lateral Geniculate Nucleus

4.2.1 Receptive Fields and Profiles of Thalamic Cells

A number of cells of visual areas elicit a spike response to a luminance signal applied on the retinal plane $M \subset \mathbb{R}^2$. Every visual neuron is characterized by its *receptive field* (RF) that is classically defined as the domain of the retina to which the neuron is sensitive. Note that in general neurons are not directly connected to the retina. For example, cortical neurons are projecting from the retina to the cortex through the lateral geniculate nucleus along the thalamic way.

The *receptive profile* (RP) of a visual neuron is defined on the domain marked by the RF, and corresponds to the impulse response of the cell as a filter kernel. It is a function $\Psi(x,y)$ (where x,y are retinal coordinates) $\Psi : M \to \mathbb{R}$ which is defined on the retinal plane M and measures the response (ON / OFF) of the neuron to stimulation at the point (x,y). When a visual stimulus $I(x,y) : M \subset \mathbb{R}^2 \to \mathbb{R}^+$ activates the retinal layer, the cells centered at every point (x,y) of M process in parallel the retinal stimulus with their receptive profile. Reverse correlation techniques enable the recording of the RPs in terms of the correlations of the inputs (generally flashes of light and dark spot) with the outputs (spikes) [18]. The correlation of the inputs with the outputs yields the transfer function of the neuron, namely the RP.

RPs of the retinal ganglion cells are usually modelled by Laplacians of Gaussians [39],

$$\Psi_0(\xi,\eta) = \Delta G(\xi,\eta),$$

where $G(\xi,\eta) = e^{-(\xi^2+\eta^2)}$ is the Gaussian bell and Δ is the standard Laplacian. The same receptive profiles are found also in the Lateral Geniculate Nucleus (LGN), that is a copy of the retina but strictly in contact with the visual cortex. The size of the retinal and LGN RPs vary with a scale parameter allowing an entire multiscale analysis of the signal. For the purpose of this study, we will consider a fixed scale, since the phenomena described are invariant with respect to size changes, up to a rescaling.

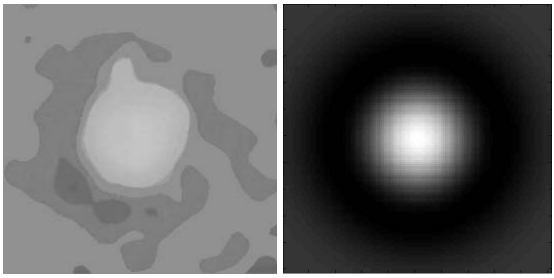

Fig. 4.1 On the left: a measured LGN cell RP (thanks to De Angelis [18]), on the right: a LGN cell RP modelled as Laplacian of a Gaussian

4.2.2 Cell Response and Lateral Connectivity of LGN

The output of the cells in LGN in response to the visual signal is highly nonlinear, and it rescales the visual input in a logarithmic way:

$$O(x,y)_{LGN} = \Delta G(x,y) * \log I(x,y).$$

The output of LGN cells is propagated via the lateral connectivity in LGN itself. Since this connectivity is isotropic [57], it can be modelled by the fundamental solution $\Gamma(x,y)$ of the 2D Laplacian operator

$$\Gamma(x,y) = -\log \sqrt{x^2+y^2}.$$

LGN lateral connectivity with strength $\Gamma(x,y)$ acts linearly on the output $O(x,y)_{LGN}$, giving a total contribution

$$\phi(x,y) = \frac{1}{2}\Big(\Gamma(x,y) * \Delta \log I(x,y)\Big). \tag{4.1}$$

Note that the action of receptive profiles $\Delta \log I(x,y)$ and the one of LGN lateral connectivity $\Gamma(x,y)*$ is dual in a differential sense.

4.2.3 The Retinex Algorithm as a Model of LGN Action

Eq. (4.1) corresponds to the Retinex algorithm in the version proposed by Horn in [31], where the authors proposed a physically based algorithm, which recovers the reflectance f of an image I as

$$\Delta \log f(x,y) = \Delta \log I(x,y), \tag{4.2}$$

where $I(x,y)$ is given. This is a Poisson equation with solution

$$\log f(x,y) = \frac{1}{2}\Big(\Gamma(x,y) * \Delta \log I(x,y)\Big),$$

formally equivalent to eq. (4.1) provided that $\phi(x,y) = log f(x,y)$.

Let us recall that the Retinex algorithm has been introduced in [37,38] to explain lightness perception, i.e. the phenomenon causing a gray patch to appear brighter when viewed against a dark background and darker when viewed against a bright background. Improvements and new models have been proposed by [35,43] among others.

In particular in [43], it has been proved that the original Retinex algorithm can be equivalently espressed by the Poisson equation (4.2), and in [26,27] a new interpretation was given in terms of covariant derivatives and fiber bundles. Indeed setting

$$\mathbf{A}(x,y) = \nabla I(x,y)/I(x,y) \tag{4.3}$$

equation (4.2) can be considered the Euler Lagrange equation of the functional

$$\tilde{F}(x,y) = \int \frac{|\nabla f(x,y) - \mathbf{A}(x,y) f(x,y)|^2}{f(x,y)^2} dxdy. \tag{4.4}$$

This functional is invariant with respect to the transformation

$$f \to fI, \quad \mathbf{A} \to \mathbf{A} + \frac{\nabla I}{I}$$

so that the choice $\mathbf{A}(x,y) = \frac{\nabla I(x,y)}{I(x,y)}$ is compatible with the transformations which leaves the functional invariant. The quantity $\nabla f - \mathbf{A} f$ can be interpreted as a covariant derivative.

Here we can further notice that, setting

$$\phi(x,y) = \log f(x,y), \quad h(x,y) = \log I(x,y), \tag{4.5}$$

equation (4.2) simplifies as

$$\Delta \phi(x,y) = \Delta h(x,y) \tag{4.6}$$

and setting as before: $\mathbf{A}(x,y) = \nabla I(x,y)/I(x,y) = \nabla h(x,y)$, the functional becomes

$$F(x,y) = \int |\nabla \phi(x,y) - \mathbf{A}(x,y)|^2 dxdy = \int |\nabla \phi(x,y) - \nabla h(x,y)|^2 dxdy, \tag{4.7}$$

while the transformations which leave the operator invariant become

$$\phi \to \phi + h, \quad \mathbf{A} \to \mathbf{A} + \nabla h.$$

The functional (4.7) has to be considered as the invariant energy underlying the Retinex Poisson equation (4.2) solved by the action of the LGN connectivity represented by eq. (4.1).

4.3 The Neurogeometrical Structure of the Primary Visual Cortex

4.3.1 The Set of Simple Cells Receptive Profiles as a Lie Group

While LGN cells are fairly isotropic, simple cells of the primary visual cortex V1 are strongly oriented, and their RPs are interpreted as Gabor patches [17, 36] or directional derivatives of Gaussians.

A first derivative of Gaussian models odd simple cell RPs (Fig. 4.2 right):

$$\Psi_0(\xi,\eta) = \partial_\eta G(\xi,\eta). \tag{4.8}$$

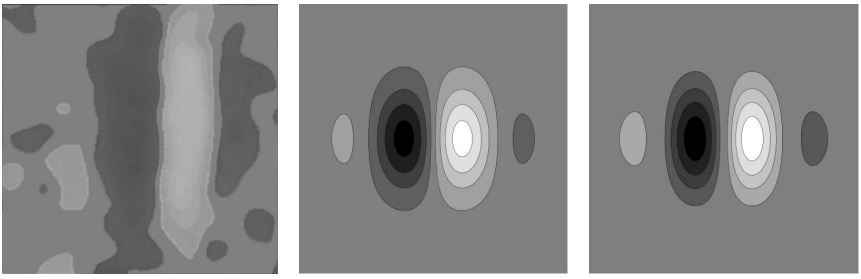

Fig. 4.2 Left: an odd simple cell RPs measured by reverse correlation techniques (thanks to De Angelis [18]). Odd receptive profile modelled as Gabor filter (middle) and first directional derivative of Gaussian (right).

The set of observed profiles can be obtained from the mother profile $\Psi_0(\xi,\eta)$ (see [36]) under the action of a Lie group.

The entire set of RPs of the same point (x,y) is then obtained by rotating the mother profile, explicitly:

$$\Psi_\theta = \Psi_0\Big(\xi\cos\theta + \eta\sin\theta, -\xi\sin\theta + \eta\cos\theta\Big).$$

This structure enlightens the modular structure of the cortex. Each family of cells acts on the same retinal basis but depends on different engrafted variables, and it is described by different groups of symmetry.

We will describe the action of the affine group of rotation and translation on vectors of R^2, since the other two groups are subset of this one. The action $M_{x,y,\theta}$ transforms every vector (ξ,η) in a new vector $(\tilde{\xi},\tilde{\eta})$ as:

$$(\tilde{\xi},\tilde{\eta}) = M_{x,y,\theta}(\xi,\eta) = \begin{pmatrix} x \\ y \end{pmatrix} + \begin{pmatrix} \cos(\theta) & -\sin(\theta) \\ \sin(\theta) & \cos(\theta) \end{pmatrix} \begin{pmatrix} \xi \\ \eta \end{pmatrix}. \tag{4.9}$$

The action of the group on the set of profiles will be:

$$\mathscr{L}_{(x_0,y_0,\theta)}\Psi(x,y) = \Psi(M^{-1}_{(x_0,y_0,\theta)}(x,y)). \tag{4.10}$$

Then the whole set of receptive profile will be $\{\Psi_{x,y,\theta}(\tilde{\xi},\tilde{\eta}) = \mathscr{L}_{(x_0,y_0,\theta)}\psi(x,y)\}$.

After rotation of the axis of an angle θ, the derivative ∂_η becomes

$$X_3 = -\sin(\theta)\partial_\xi + \cos(\theta)\partial_\eta. \tag{4.11}$$

Then the odd cell RP oriented in the direction θ is in general represented by

$$\Psi_\theta = X_3 G(\xi,\eta). \tag{4.12}$$

Finally the expression of filters on different points is obtained by translation:

$$\Psi_{x,y,\theta}(\tilde{x},\tilde{y}) = \Psi_\theta(x-\tilde{x},y-\tilde{y}).$$

In Fig. 4.3 we visualize the set of odd simple cells.

Note that for simplicity we take Euclidean translations on the cortical plane neglecting the conformal log-polar retino-cortical mapping, that can be easily taken into account by introducing a Riemannian metric on the cortical layer. This feature will not be implemented in the present study.

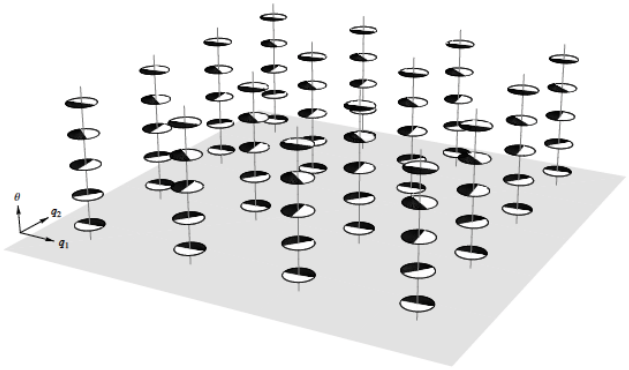

Fig. 4.3 The set of simple cells odd receptive profiles $\Psi_{x,y,\theta}(\tilde{x},\tilde{y})$ represented in the space (x,y,θ)

4.3.2 Simple Cells Response

If classical RPs are considered, the output u is given by linear filtering of the stimulus $h(\xi,\eta) = log(I(\xi,\eta))$ by the set of RPs:

$$u(x,y,\theta) = \int_M h(\tilde{\xi},\tilde{\eta})\Psi_{(x,y,\theta)}(\tilde{\xi},\tilde{\eta})d\tilde{\xi}d\tilde{\eta} \tag{4.13}$$

and by eq. (4.12)

$$u(x,y,\theta) = \int X_3 G(\xi,\eta)h(\tilde{\xi},\tilde{\eta})d\tilde{\xi}d\tilde{\eta} = -X_3 G(\xi,\eta) * h(\tilde{\xi},\tilde{\eta}) = -X_3(\theta)h_s \tag{4.14}$$

where h_s is a smoothed version of h,

$$h_s = h * G(\xi,\eta).$$

4.3.3 Non Maximal Suppression

For a fixed point (x,y) the output is a function just of the variable θ that attains its maximum at the point

$$\max_{\theta} ||u(x,y,\theta)|| = ||u(x,y,\bar{\theta})||. \tag{4.15}$$

This maximality condition can be mathematically expressed requiring that the derivative of $||u||$ with respect to the variables θ vanishes at the point $(x,y,\bar{\theta})$:

$$\partial_\theta u(x,y,\bar{\theta}) = 0. \tag{4.16}$$

At the maximum point $\bar{\theta}$ the derivative with respect to θ vanishes, and we have

$$0 = \frac{\partial}{\partial\theta}u(x,y,\bar{\theta}) = \frac{\partial}{\partial\theta}X_3(\bar{\theta})I = -X_1(\bar{\theta})I = -\langle X_1(\bar{\theta}),\nabla I\rangle \tag{4.17}$$

where

$$X_1(\theta) = cos(\theta)\partial_\xi + sin(\theta)\partial_\eta.$$

The condition (4.17) means that the vector $(\cos(\bar{\theta}),\sin(\bar{\theta}))$ is orthogonal to the gradient of h (and to the gradient of I) and then is tangent to its level lines. *Then the angle $\bar{\theta}$ maximizing the output indicates the direction of level lines of the stimulus image.*

Calling

$$\bar{\rho}(x,y) = ||u(x,y,\bar{\theta}(x,y))||, \tag{4.18}$$

we can say that the point (x,y) is lifted to the point $(x,y,\bar{\theta}(x,y),\bar{\rho}(x,y))$ in the cortical space (x,y,θ,ρ). With the same procedure it is possible to lift all the level lines of the 2D image I into 4D curves.

It is easy to check (see for example [12]) that the first 3 components of the lifted curves are tangent to the plane generated by the vector fields

$$\mathbf{X}_1 = (\cos(\theta),\sin(\theta),0) \quad \mathbf{X}_2 = (0,0,1). \tag{4.19}$$

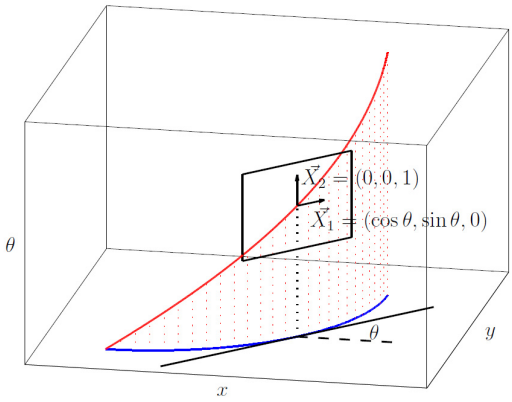

Fig. 4.4 A level line of the image (in blue) and its 3D cortical lifting (in red). The tangent vector to the blue curve is $(\cos(\theta), \sin(\theta))$, so that the tangent vector to its lifting lies in the plane generated by $\mathbf{X}_1 = (\cos(\theta), \sin(\theta), 0)$ and $\mathbf{X}_2 = (0,0,1)$.

and visualized in Fig. 4.5. In Fig. 4.4 we depicted the 3D section with the plane (x, y, θ).

Let us notice that all admissible curves of the cortical space are tangent at every point to the subspace generated by $\mathbf{X}_1$ and $\mathbf{X}_2$, which has dimension 2. In the standard Riemannian setting, the number of generators of the tangent space equal the dimension of the space, while in the geometrical model of cortical space the dimension of the manifold is 3, and the admissible tangent space has dimension 2. This endows the 3D space $R^2 \times S^1$ of the variables (x, y, θ) with a sub-Riemannian geometry. While no constraint is imposed on the last variable ρ, the vector field in the ρ direction will be

$$\mathbf{X}_4 = (0,0,0,1).$$

The full 4D space will consequently be

$$R^2 \times S^1 \times R^+,$$

with a sub-Riemnnian metric in the first 3 variables, and a standard metric in the last variable. Since the geometry on the last component ρ is standard, we will describe the geometry of the 3D space generated by the first 3 variables (x, y, θ).

4.3.4 Association Fields and Integral Curves of the Structure

Field, Heyes and Hess in [23] have shown the existence of a perceptual field connecting patches of position and orientation, see Fig. 4.6 left. This connectivity pattern, called association field, is considered at the base of the constitution of

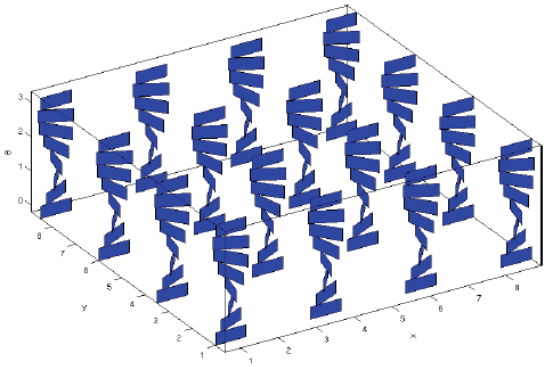

Fig. 4.5 The bundle of subspaces of the tangent manifold generated by the fields $\mathbf{X}_1(\theta)$ and $\mathbf{X}_2(\theta)$

boundaries in visual perception, implementing the gestalt law of good continuation. We have shown in [13] that the association field is well modelled by the integral curves of the vector fields $\mathbf{X}_1$ and $\mathbf{X}_2$, starting from a fixed point (x_0, y_0, θ_0):

$$\begin{aligned} \gamma'(t) &= (x'(t), y'(t), \theta'(t)) = \mathbf{X}_1(x(t), y(t), \theta(t)) + k\mathbf{X}_2(x(t), y(t), \theta(t)) \quad (4.20) \\ \gamma(0) &= (x_0, y_0, \theta_0), \end{aligned}$$

A fan of such integral curves by varying the parameter k is visualized in Fig. 4.6 right.

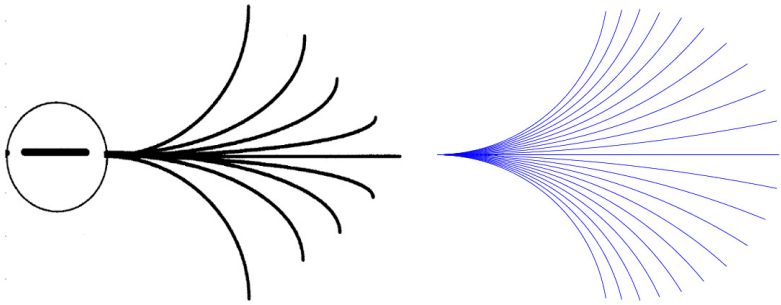

Fig. 4.6 The association fields of Fields, Heyes and Hess [23] (left) and the projected integral curves with constant coefficients (right)

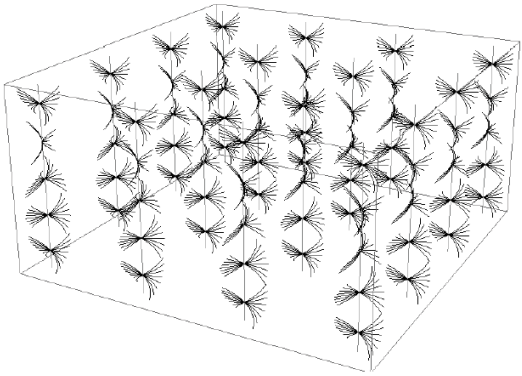

Fig. 4.7 The constant coefficient integral curves of the fields $\mathbf{X}_1(\theta)$ and $\mathbf{X}_2(\theta)$, modeling the local connectivity between points of the cortical space

4.3.5 Length of Lifted Curves and Geodesics

A 2D level line

$$\tilde{\gamma} = (x(t), y(t))$$

parametrized by arc length t, has tangent vectors

$$(x'(t), y'(t)) = (\cos(\theta(t)), \sin(\theta(t)))$$

at every point, where θ denotes the direction of the curve at the point $(x(t), y(t))$. We have seen that the action of simple cells lifts the level line into a 3D cortical curve $\gamma(t) = (x(t), y(t), \theta(t))$. Differentiating x and y we get

$$(x''(t), y''(t)) = (-\sin(\theta(t))\theta'(t), \cos(\theta(t))\theta'(t)) = (-y'(t), x'(t))\theta'(t)$$

so that the euclidean curvature can be computed as

$$k = \frac{y''x' - x'y''}{((x')^2 + (y')^2)^{3/2}} = \theta'$$

The length of the lifted curve is

$$L(\gamma(t)) = \int \sqrt{x'(t)^2 + y'(t)^2 + \theta'(t)^2}\, dt = \int \sqrt{1 + k(t)^2}\, dt,$$

considering that $x'(t)^2 + y'(t)^2 = 1$. Notice that the length of lifted curves depends on the length of the 2D level line and on its curvature, analogous to the case of the elastica functional $\int (1 + k(t)^2) dt$, introduced by David Mumford in [44]. The distance between two cortical points (x, y, θ) and $(\bar{x}, \bar{y}, \bar{\theta})$ is defined in term of the length functional as

$$d((x,y,\theta),(\bar{x},\bar{y},\bar{\theta})) = \inf\{L(\gamma) : \gamma \text{ is an horizontal curve} \quad (4.21)$$
$$\text{connecting } (x,y,\theta) \textit{ and } (\bar{x},\bar{y},\bar{\theta})\},$$

see [13]. In other words the horizontal path on which the infimum is achieved is a geodesic curve of the cortical space. As suggested by Petitot and Tondout in [46], subjective contours can be computed as geodesics curves in a contact structure. Here we can show (see Fig. 4.8) that subjective contours can be well represented by sub-Riemannian geodesics in the $SE(2)$ group, i.e. as minimizers of (4.21).

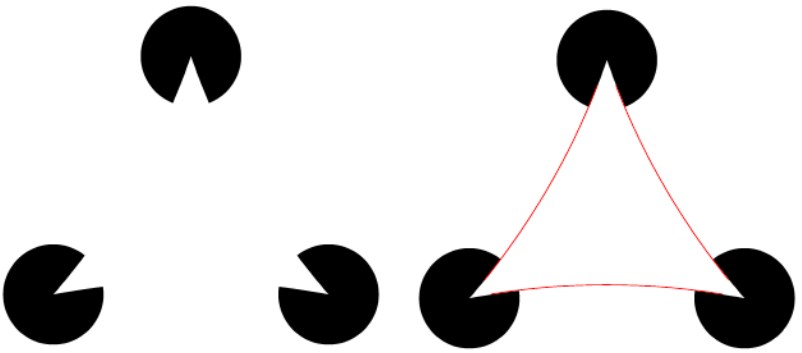

Fig. 4.8 A Kanizsa triangle with curved boundaries (left) and the subjective contours modelled as geodesics of the cortical space (right). The geodesics are not rectilinear, since they minimize the distance (4.21), which is a function of the curvature k.

4.4 The Cortical Implementation of the Neurogeometrical Structure

4.4.1 Response of Simple Cells and Bargmann Transform

Daugmann in [17] first proved that the shape of the simple cells is intimately related to their functionality. His crucial remark is the fact that simple cells try to localize at the same time position (x,y) and frequency ω. Hence the set $SE(2)$ can be interpreted as a real manifold of the phase space, with the frequency variables expressed in polar coordinates:

$$SE(2) \subset \mathbb{C}^2 = \{(x,y,|p|\cos(\theta),|p|\sin(\theta))\}.$$

The classical uncertainty principle in the Heisenberg space asserts that it is not possible to detect with arbitrary precision both position and momentum (see [15]). The principle also provides an explicit condition for functions that minimize uncertainty with respect to the position and momentum operators. These minimizers are called coherent states, and in the Heisenberg setting they are the Gabor filters. This is why

these filters have been proposed in [17] as models for the shape of receptive profiles (see Fig. 4.2 Middle). The complete set of coherent states can be obtained via the action of the group (4.10) on a fixed mother state Ψ . Recall that, if Ψ is a coherent state, the Bargmann transform of the function h is

$$B_\Psi(h)(x,y,\theta) = \int \mathscr{L}_{(x,y,\theta)}\Psi(\tilde{x},\tilde{y})h(\tilde{x},\tilde{y})d\tilde{x}d\tilde{y}. \tag{4.22}$$

Hence the response of the filters on an image defined in (4.13) can be interpreted as a Bargmann transform (see [4] for the definition and [3] for this interpretation of the cell response).

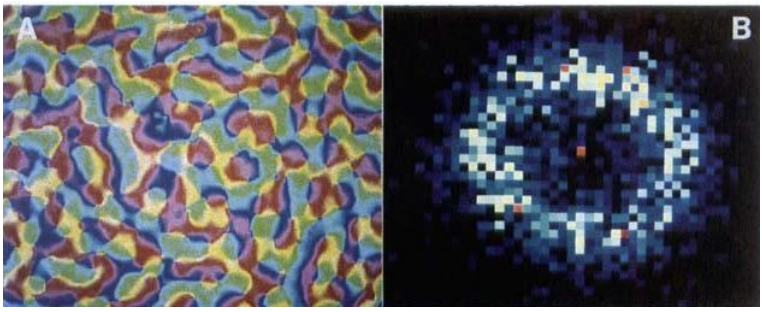

Fig. 4.9 A pinwheel map (left) and its spectral behavior (right). Figure extracted from [41].

4.4.2 The Activity Maps and the Pinwheel Structure

Even if the primary visual cortex shows the symmetries of SE(2), that is a 3-dimensional group, its physical implementation is realized on the 2-dimensional layer provided by the cortex. Orientation columns are radially arranged around singular points like the spokes of a wheel, that are called pinwheels (see Fig. 4.9). This structure has been observed first with optical imaging techniques [6, 5] and more recently by in vivo two-photon imaging proving their organization with single cell precision. In [41] an empirical method was also introduced that is able to reproduce orientation map-like structures as a superposition of plane waves with random phases. More recently, in [16], the activity in V1 has been reconstructed by measuring cell responses to so called gratings. Activated regions depend on the orientation at which they are presented so that if a family of gratings is presented to an observer, the result is a family of real maps $\{u_\theta(x,y)\}$ (see Fig 4.10). The pinwheel image has been reproduced in Fig.4.10 (center) by performing a vector sum of the orientations

$$\mathscr{P}(x,y) = \frac{1}{2}arg\int_0^\pi e^{i2\theta}u_\theta(x,y)d\theta. \tag{4.23}$$

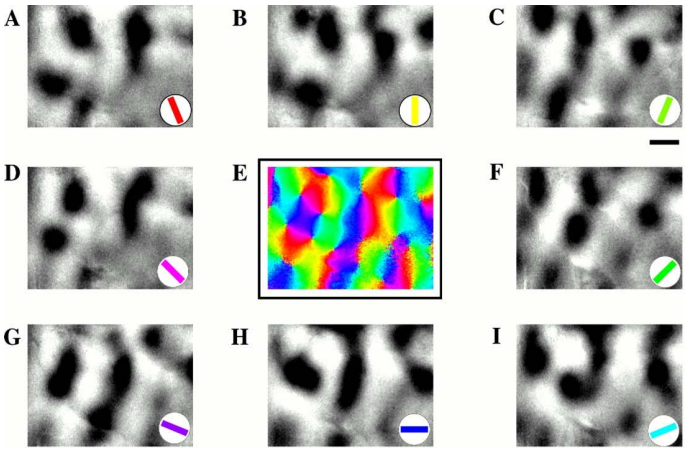

Fig. 4.10 The original results obtained by [16] showing a set of gray level cortical maps u_θ acquired by optical imaging and the reconstructed color coded image at the center with the well known pinwheel structure

4.4.3 An Uncertainty Principle on the Functional Geometry

In a recent paper [2] Barbieri, Sanguinetti and the authors of the present paper proposed a model of the cortical activity and pinwheel structure based on an uncertainty principle in the structure $SE(2)$ of the visual cortex, which reproduces the experiment in [16]. The image of the left-invariant vector fields (4.19) under the differential of the action defined in (4.10) is defined as $Y_i = d\mathscr{L}(X_i)$ and provides the differential operators

$$Y_1 = \partial_{\tilde{y}}, \quad Y_2 = \tilde{y}\partial_{\tilde{x}} - \tilde{x}\partial_{\tilde{y}}. \tag{4.24}$$

Under the action of the Fourier transform, these vector fields (4.24) become respectively

$$\mathscr{F}(Y_1 f) = i\xi_2 \hat{f}, \quad \mathscr{F}(Y_2 f) = (\xi_2 \partial_{\xi_2} - \xi_1 \partial_{\xi_2})\hat{f}.$$

Experimentally we see that the Fourier spectrum of the orientation maps is approximately concentrated on a circle (see Fig.4.9, right). On the other hand no action is performed by the fields in the radial direction, allowing to restrict the study to functions defined on the circle of radius ρ (see [55]). Since it is not possible to further reduce the set where to study these vector fields, the representation of these vector fields on the circle is called irreducible. In polar coordinates $(\xi_1, \xi_2) = \rho(\cos(\tilde{\theta}), \sin(\tilde{\theta}))$ they reduce to an even simpler representation:

$$\hat{Y}_1 \hat{f} = i\rho \sin(\tilde{\theta})\hat{f}, \quad \hat{Y}_2 \hat{f} = \partial_{\tilde{\theta}} \hat{f}. \tag{4.25}$$

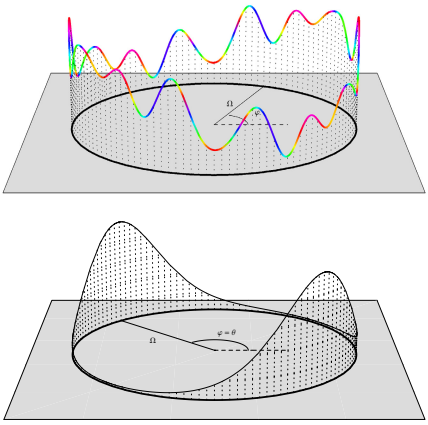

Fig. 4.11 Top: A general function in the reduced Fourier plane, where only a circle is considered. The height of the graph represents the modulus, and the color represents the argument of the function. Bottom: A coherent state in the reduced Fourier plane.

The uncertainty principle can be stated for any couples of noncommuting self-adjoint operators on Hilbert spaces [24]. In terms of operators $\hat{Y}_i$ it reads:

$$|\langle \hat{\Phi}, \rho\cos(\tilde{\theta})\hat{\Phi}\rangle| \leq 2\|\rho\sin(\tilde{\theta})\hat{\Phi}\|\ \|\partial_{\tilde{\theta}}\hat{\Phi}\|. \tag{4.26}$$

Minimal uncertainty states can be computed by making use of an equation associated to inequality (4.26), that in this case reads (see also [9])

$$(\hat{Y}_2 - i\lambda\hat{Y}_1)\hat{\Phi}(\tilde{\theta}) = 0 \tag{4.27}$$

where the scaling parameter λ represents frequency. Solutions to equation (4.27) read, up to a normalization constant $c = c_\rho(\lambda)$

$$\hat{\Phi}(\tilde{\theta}) = ce^{\lambda\rho\cos(\tilde{\theta})}. \tag{4.28}$$

The states (4.28) are the most concentrated functions in angular position and momentum, hence allowing optimal localization (from now on we will omit to write the constant c for simplicity). Note that the bigger λ is, the sharper its localization is: for large values of λ, that means $\lambda \gg 1/\rho$, it is maximally concentrated. Due to the uncertainty inequality, the variance of $\frac{d}{d\varphi}$ grows to infinity, i.e. it is maximally undetermined. On the other hand, for small values of λ, i.e. $\lambda \ll 1/\rho$, then $\hat{\Phi}(\varphi)$ approaches a constant, and the angular momentum is maximally concentrated.

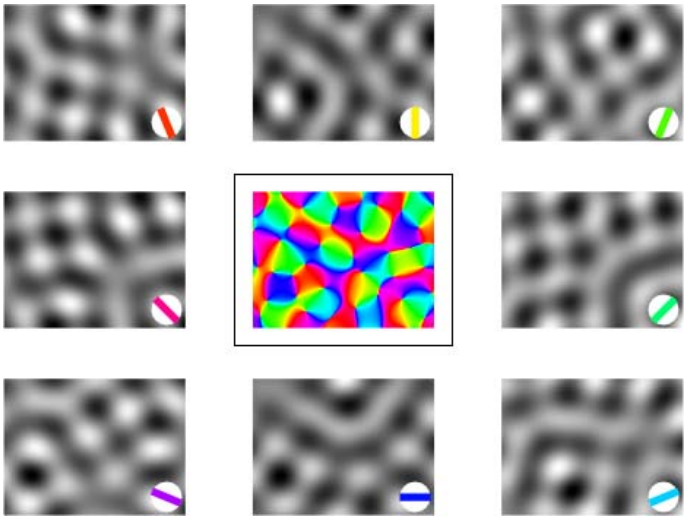

Fig. 4.12 The gray valued maps $u_{\Phi,\theta}(x,y)$ for different values of the orientation and in center the color image obtained as a vector sum, to be compared with the experimental result of [16], reproduced in Fig.4.10

4.4.4 Irreducible Bargman Transform, the Activity Maps and Pinwheels

The notion of Bargmann transform in $SE(2)$ has been introduced by Barbieri et al. in [3]. In analogy with the classical expression in (4.22) it is expressed as the operator associated to the coherent states. The action of the group on the coherent states Φ is the Fourier transform of the action defined in (4.10):

$$\hat{\mathscr{L}}_{(x,y,\theta)}\hat{\Phi}(\tilde{\theta}) = e^{-i\rho_0(x\cos(\tilde{\theta})+y\sin(\tilde{\theta}))}\hat{\Phi}(\tilde{\theta}-\theta).$$

Consequently, the irreducible Bargman transform reads:

$$B_\Phi(h)(x,y,\theta) = \int_{S^1} \hat{\mathscr{L}}_{(x,y,\theta)}\hat{\Phi}(\tilde{\theta})h(\tilde{\theta})d\tilde{\theta}. \tag{4.29}$$

Given a white noise $W = W(\tilde{\theta})$ with values in $[0,2\pi]$, defined on $[0,2\pi]$, and such that $W(\tilde{\theta}+\pi) = -W(\tilde{\theta})$ we can consider the function $B_\Phi(W)(x,y,\theta)$. We impose the symmetries of the cortex to represent orientations. Namely we require that it is $\pi-$periodic in θ and provides opposite response at orthogonal angles as is the case for V1 cells:

$$u_{\Phi,\theta}(x,y) = Re\Big(B_\Phi(W)(x,y,\theta) - B_\Phi(W)(x,y,\theta+\pi/2)\Big). \tag{4.30}$$

By definition this irreducible Bargmann transform is simply the transform in (4.22) restricted to functions with constant frequency. Hence it expresses a response of the cortex, which has been interpreted in [2] as a model of the activity maps measured in [16](see Fig. 4.12). As in (4.23) we perform the sum

$$\mathscr{P}_{\Phi}(x,y) = arg\Big(\int_0^{\pi} u_{\Phi,\theta}(x,y)e^{i2\theta}d\theta\Big) \tag{4.31}$$

reproducing the original experiment. An important property of (4.31) is that it can be represented as a sum of plane waves, with frequency ρ, and random phases in accordance with the mechanism introduced in [41]. This model is indeed able to interpret both the orientation activity maps and the pinwheel-shaped orientation maps as interference figures.

4.4.5 Propagation in the Pinwheel Structure

Techniques of optical imaging associated to tracers allow a large-scale observation of neural signal propagation via cortico-cortical connectivity. These tests have shown that the propagation is highly anisotropic and almost collinear to the preferred orientation of the cell (see Fig. 4.13), confirming at neural level the phenomenological results of Field, Heyes and Hess in [23] and the model of propagation curves developed in section 3. This experiment suggests to introduce not only a propagation along curves but with a differential operator, which can propagate in a neighborhood of a point. Even though the propagation is performed in the cortex at the pinwheel level, we will describe the neural propagation in the 3D model of $R^2 \times S^1$, which is formally simpler to handle, and from which it is possible to project on the pinwheel structure.

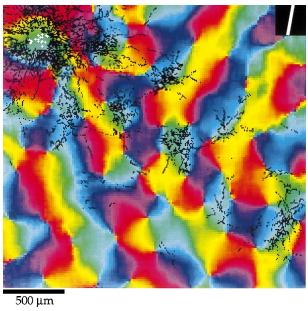

Fig. 4.13 A marker is injected in the cortex, in a specific point, and it diffuses mainly in regions with the same orientation as the point of injection

4.5 Propagation in the Family of Simple Cells

4.5.1 Propagation along the Association Fields

Neural activity develops and propagates only along the integral curves of the structure. If γ is one of the curves in (4.20), the Lie derivative of a function f along the curve γ is defined as

$$X_i u(\xi_0) = \frac{d}{ds}(u \circ \gamma)_{|s=0},$$

and on regular functions it coincides with the directional derivative. In analogy with the Euclidean gradient, the sub-Riemannian gradient is defined by

$$\nabla_R u = (X_1 u, X_2 u).$$

Note that it does not contain derivatives in direction X_3, which can be recovered by commuting:

$$X_3 = [X_2, X_1] = X_2 X_1 - X_1 X_2,$$

see [12] for details. Hence X_3 will play a role similar to a second derivative. In this setting the divergence of a horizontal vector field $v = (v_1, v_2)$ is defined as

$$div_R v = X_1 v_1 + X_2 v_2,$$

so that the sub-Laplacian operator becomes

$$\Delta_R u = div_R(\nabla_R u) = X_{11} u + X_{22} u. \tag{4.32}$$

The time dependent counterpart is the sub-Riemnnian diffusion operator:

$$\partial_t u = \Delta_R u, \tag{4.33}$$

modelling a diffusive mechanism of propagation in the cortical space.

4.5.2 The Lifting Mechanism of the Whole Image: Regular Graphs in $R^2 \times S^1$

The mechanism of non maxima suppression does not lift each level lines independently, but the whole image is lifted to a surface. Condition (4.16) ensures that the lifted surface is identified by a zero level set of the function

$$H(x, y, \theta) = \partial_\theta u(x, y, \theta),$$

meaning that if we consider only strict maxima, the lifted surface becomes

$$\Sigma = \{(x, y, \theta) : H(x, y, \theta) = 0, \partial_\theta H(x, y, \theta) > 0\}. \tag{4.34}$$

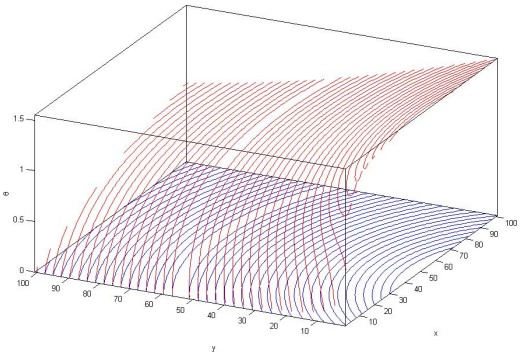

Fig. 4.14 The level lines of a 2D image (in blue), and their 3D lifting (in red)

Since the vector ∂_θ is a horizontal vector, then Σ is a regular surface in the sub-Riemannian metric.

In particular, we can define a horizontal normal to Σ, and denote with ν_R its projection on the horizontal plane of the Euclidean normal:

$$\nu_R = \frac{(X_1 u, X_2 u)}{\sqrt{(X_1 u)^2 + (X_2 u)^2}}.$$

In analogy with the notion of Euclidean curvature, we define the sub-Riemannian curvature as the $R-$divergence of the $R-$normal vector:

$$H_R(\Sigma) = div_R(\nu_R),$$

4.5.3 *Completion Model and Minimal Surfaces in the Roto-translation Space*

The two cortical mechanisms of sub-Riemannian diffusion (4.33) and non maximal suppression (4.34) will be iteratively applied. The action of these two mechanism can be formalized as a two step algorithm.

- The lifted surface $\Sigma_0 = \Sigma$ defined in (4.34) and the function $\rho_0(x,y) = \rho(x,y)$ defined on it in (4.18) allow to define a measure $\rho_0 \delta_{\Sigma_0}$ concentrated on the surface. Diffusing this measure, we define a function $u_1(x,y,\theta,t)$ concentrated in a neighborhood of the surface.
- The second step is a non maximal suppression, which performs a concentration and allows recovering a surface Σ_1 via the condition $\partial_\theta u = 0$ and a new function $\rho_1 = u_{|\Sigma_1}$ .The surface Σ_1 will be the graph of a function θ_1 .

To the new surface we iteratively apply the same two step procedure.

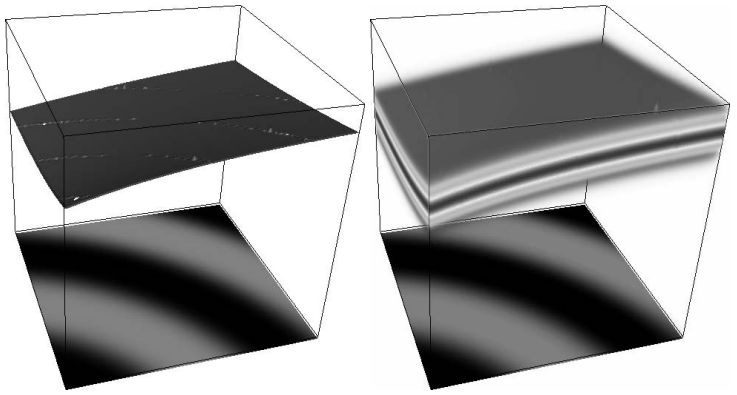

Fig. 4.15 The two step algorithm: the lifted surface generated by a concentration mechanism (left), and its diffusion (right)

If we fix a time T and a discretization step $h = T/m$, we repeat m times the algorithm. At a general step n we will have a surface Σ_n and a function ρ_n, defined on Σ_n. We diffuse for an interval of time of length h:

$$\begin{cases} \partial_t u = \Delta_R u \; in (\mathbb{R}^2 \times S^1) \backslash \Sigma_0 \quad t \in [nh, (n+1)h] \\ u(\cdot, nh) = \rho_n \delta_{\Sigma_n}. \end{cases} \tag{4.35}$$

At time $t = (n+1)h$ we have a new function ρ_{n+1} and a new surface defined as

$$\rho_{n+1}(\cdot, (n+1)h) = u(\cdot, (n+1)h) \quad \text{and} \quad \Sigma_{n+1}((n+1)h) = \{\partial_\theta u = 0, \partial^2_\theta u < 0\}.$$

After m steps we have two sequences: $\rho_{m+1}(\cdot, T)$ and $\Sigma_{m+1}(T)$. Letting m go to $+\infty$ we have:

$$\rho(T) = lim_{m \to +\infty} \rho_{m+1}(T), \quad \Sigma(T) = lim_{m \to +\infty} \Sigma_{m+1}(T)$$

The diffusion followed by a concentration in the normal direction leads to a purely tangential diffusion of the surface giving rise to the surface $\Sigma(T)$ moving by curvature, with initial surface Σ_0. The function $\rho(T)$ coincides with the Laplace Beltrami flow, with initial condition ρ_0.

This mechanism is a generalization of the well known algorithm of Merriman, Osher and Sethian in [42]. The convergence of the Euclidean version of this scheme has been proved by Evans [22] and Barles, Georgelin [5]. The convergence of the analogous flow in the sub-Riemannian setting has been first presented in [13] and then formalized in [10].

For $T \to +\infty$ the surface $\Sigma(T)$ converges to a minimal surface Σ, and $\rho(T)$ tends to the solution $\rho(x, y)$ of the (time independent) Laplace Beltrami equation on the surface.

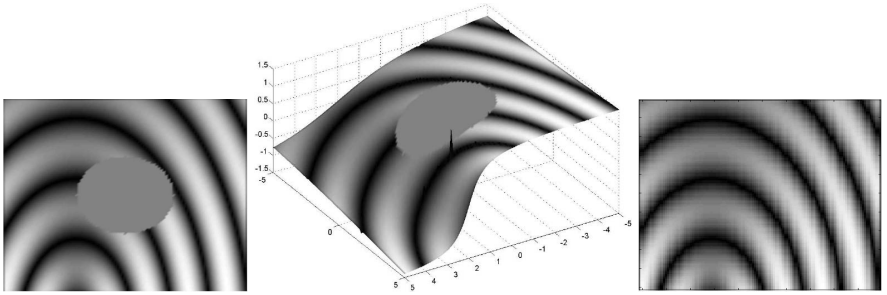

Fig. 4.16 An image with a missing part (left) is lifted to the 3D space (middle) and completed with the previous described algorithm (right)

The algorithm gives rise to an amodal completion of the image. Indeed the initial image (see Fig. 4.16), left) is lifted in the rotranslation space. The lifted surface is completed by iteratively applying the algorithm until a minimal surface is generated.

4.5.4 Minimal Surfaces as Minima of the Area Functional

The minimal surface Σ can be expressed as a graph of a function θ. In addition, if we project the vector fields defined in (4.19) on the x,y plane, we end up with a unique vector field

$$X_{1\theta} = cos(\theta(x,y))\partial_x + \sin(\theta(x,y))\partial_y = \langle \nabla, (\cos(\theta(x,y)), \sin(\theta(x,y)))\rangle \quad (4.36)$$

since the projection of the vector X_2 on the same plane is 0. We explicitly note that the vector $X_{1\theta}$ here is only formally similar to the vector X_1 in (4.19). Indeed $\theta(x,y)$ in (4.36) is a function while in (4.19) θ was simply an independent variable of the 3D space.

The minimal surfaces equation can be expressed in terms of the function $\theta(x,y)$ as follows:

$$X_{1\theta}\Big(\frac{\rho^2 X_{1\theta}\theta(x,y)}{\sqrt{|\rho^2 X_{1\theta}\theta(x,y)|^2+1}}\Big) = 0,$$

where θ coincides with $\bar{\theta}$ on the existing boundaries. Taking explicitly the derivative, the equation becomes

$$X_{1\theta}(\rho^2 X_{1\theta}\theta(x,y)) = 0. \quad (4.37)$$

This equation can be interpreted as a second order directional derivative, in the direction $(\cos(\theta), \sin(\theta))$. Hence it is the Euler-Langrange equation of the Dirichlet functional

$$\int |X_{1,\theta}\theta(x,y)|^2 \rho^2(x,y)dxdy.$$

The function ρ satisfies the Laplace Beltrami equation, which is the Euler-Langrange equation of the functional

$$\int |X_{1,\theta}\rho(x,y)|^2 dxdy.$$

Summing these two terms we obtain

$$\int |X_{1,\theta}\theta(x,y)|^2\rho^2(x,y)dxdy + \int |X_{1,\theta}\rho(x,y)|^2 dxdy. \tag{4.38}$$

In order to take into account the graphs of the two functions θ and ρ we can define a function

$$\mathbf{A}(x,y) = \rho(x,y)(\cos(\theta(x,y)), \sin(\theta(x,y)).$$

In (4.18) we defined ρ as the modulus of the gradient and θ as its orientation. Then, if we denote $\mathbf{A} = (A_1, A_2)$ the derivative X_1 is expressed in terms of $\mathbf{A}$ as

$$X_{1,A} = \frac{A_1}{\sqrt{A_1^2 + A_2^2}}\partial_x + \frac{A_2}{\sqrt{A_1^2 + A_2^2}}\partial_y,$$

and the functional in (4.38) can be expressed in terms of the function $\mathbf{A}$ as

$$\int |X_1\mathbf{A}|^2 dxdy. \tag{4.39}$$

Indeed

$$\int |X_1A_1|^2 = \int |X_1(\rho cos(\theta))|^2 = \int (X_1\rho cos(\theta) + \rho sin(\theta)X_1\theta)^2 =$$

$$= \int (X_1\rho)^2 cos^2(\theta) + \rho^2 sin^2(\theta)(X_1\theta)^2 + 2\rho X_1\rho cos(\theta)sin(\theta)X_1\theta$$

$$\int |X_1A_2|^2 = \int (X_1\rho)^2 sin^2(\theta) + \rho^2 cos^2(\theta)(X_1\theta)^2 - 2\rho X_1\rho cos(\theta)sin(\theta)X_1\theta.$$

Summing up we get

$$\int |X_1\mathbf{A}|^2 = \int (X_1\rho)^2 + \rho^2(X_1\theta)^2.$$

4.6 A Field Lagrangian for Perceptual Completion

4.6.1 The Full Lagrangian

In this section we will study the joint action of LGN cells and cells in V1, taking into account feed-forward, horizontal and feedback connectivity. We propose a complete Lagrangian, sum of three terms: a particle term corresponding to functional (4.7), a

field term modelled by functional (4.39), and an interaction term coupling the two terms as in the usual Lagrangian field theories.

The first term is

$$\mathscr{L}_1 = \int |\nabla\phi(x,y) - \nabla h(x,y)|^2 dxdy \tag{4.40}$$

and is directly inspired by the Retinex model, describing the reconstruction of the image from image boundaries. It is considered here as the particle term of the Lagrangian, where $\phi(x,y)$ is the particle and $h(x,y)$ is the stimulus forcing term.

The field term is the functional (4.38), in analogy with the classical fields theories:

$$\mathscr{L}_2 = \int |X_1\mathbf{A}|^2 dxdy.$$

It expresses the spatial propagation of the field $\mathbf{A}(x,y)$ where $\mathbf{A}$ denotes the presence of subjective contours. As we have seen in chapter 4.5, the propagation of level lines (and then of subjective contours) is a strongly anisotropic process, and it is performed with respect to a sub-Riemannian metric, hence the functional is expressed in terms of the vector field X_1.

The last term describes the interaction between the particle $\phi(x,y)$ and the field $\mathbf{A}(x,y)$. In classical physics it is called "minimal coupling" because it tries to minimize the difference between the two terms:

$$\mathscr{L}_3 = \int |\nabla\phi(x,y) - \mathbf{A}(x,y)|^2 dxdy. \tag{4.41}$$

The field $\mathbf{A}(x,y)$ codifies illusory contours. When $\mathbf{A}(x,y)$ is viewed as a forcing term for $\phi(x,y)$, this second term is similar to the Retinex term (4.40) but driven by subjective contour instead of existing ones, while when $\Phi(x,y)$ is viewed as a forcing term for $\mathbf{A}(x,y)$, it drives the constitution of subjective contours.

The resulting functional $\mathscr{L} = \mathscr{L}_1 + \mathscr{L}_2 + \mathscr{L}_3$ is then

$$\mathscr{L} = \int |\nabla\phi - \nabla h|^2 dxdy + \int |\nabla\phi - \mathbf{A}|^2 dxdy + \int |X_1\mathbf{A}|^2 dxdy \tag{4.42}$$

where all the terms are functions of the coordinates (x,y).

4.6.2 The Euler Lagrange Equations

The Euler Lagrange Equations of the functional (4.42) are obtained by variational calculus:

$$\begin{cases} \Delta\phi = \frac{1}{2}(\Delta h + div(\mathbf{A})) \\ \Delta_{\mathbf{A}}\mathbf{A} = -\nabla\phi + \mathbf{A}. \end{cases} \tag{4.43}$$

The first equation (particle equation) is clearly a generalized Retinex equation, forced by the boundaries present in the stimulus Δh and by the subjective boundaries $div(\mathbf{A})$. It performs a contrast invariant reconstruction of the image. Note that the two terms $\mathscr{L}_1$ and $\mathscr{L}_2$ which generalize the Retinex functional give rise to this unique particle equation.

The second equation propagates boundaries in the sub-Riemmanian metric, and allows to recover subjective boundaries. Note that $\mathbf{A} = (A_x, A_y)$ is a vector, hence the first equality is indeed a system, and the sub-Riemannian Laplacian $\Delta_{\mathbf{A}}$ is the directional Laplacian associated to the considered metric.

We explicitly remark that the equation of $\mathbf{A}$ is a non-linear sub-Riemannian equation, and can be solved by iterative linearization.

This means that we need to find an initial approximated solution $\mathbf{A}_0$. A natural choice is the solution of the vector Laplace equation

$$\Delta \mathbf{A}_0 = \nabla \phi.$$

Of course this is only an approximated solution $\mathbf{A}_0$, but we can recover a better one $\mathbf{A}_1$ as a solution of

$$\Delta_{\mathbf{A}_0} \mathbf{A}_1 = \nabla \phi,$$

using the sub-Riemmannian operator associated to $\mathbf{A}_0$. From here we start an iteration:

$$\Delta_{\mathbf{A}_1} \mathbf{A}_2 = \nabla \phi, \cdots \quad \Delta_{\mathbf{A}_{j-1}} \mathbf{A}_j = \nabla \phi.$$

At each step we get a better approximation of the solution, moreover the sequence has a limit $\mathbf{A} = \lim_{j \to +\infty} \mathbf{A}_j$. Passing to the limit in the previous expression, we will get:

$$\Delta_{\mathbf{A}} \mathbf{A} = \nabla \phi,$$

so that the limit provides a solution of the nonlinear equation.

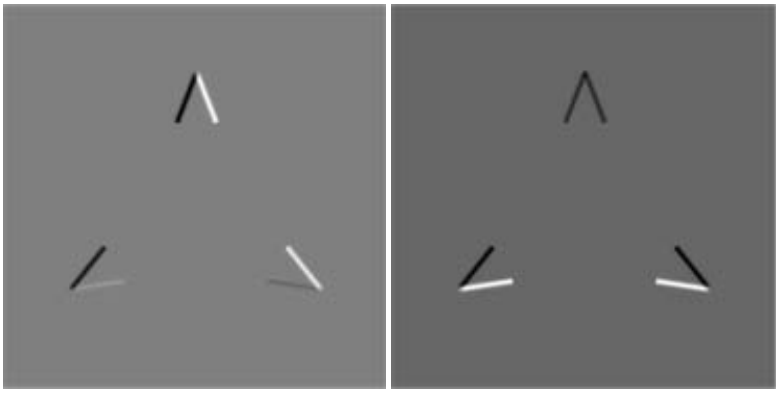

Fig. 4.17 The x and y components of ∇h related to the Kanizsa triangle inducers

4.6.3 Solution of Euler Lagrange Equations

We solve sequentially the coupled system of differential equations (4.43). We first apply the Retinex equation to the initial image:

$$\Delta\phi = \frac{1}{2}\Delta h \tag{4.44}$$

and solve it by linear convolution

$$\phi = \frac{1}{2}\Big(\Gamma(x,y) * \Delta h\Big)$$

with the fundamental solution of the 2D Laplacian:

$$\Gamma(x,y) = -\log|(x,y)|.$$

Then we solve the equation for boundaries propagation. In this first step, we choose $\mathbf{A} = 0$ in the right hand side, and the nonlinear equation reduces to

$$\Delta_{\mathbf{A}}\mathbf{A} = \nabla\phi.$$

As we explained in the previous section, this equation will be solved by linearization, stopped after the first two steps:

$$\begin{cases} \Delta\mathbf{A}_0 = \nabla\phi \\ \Delta_{\mathbf{A}_0}\mathbf{A}_1 = \nabla\phi. \end{cases} \tag{4.45}$$

The first term is computed by convolution

$$\mathbf{A}_0 = \overrightarrow{\Gamma} * \nabla\phi,$$

where $\overrightarrow{\Gamma}$ is the fundamental solution of the vector Laplacian

$$\overrightarrow{\Gamma}(x,y) = (-\log|(x,y)|, -\log|(x,y)|).$$

The second one is computed by approximating functions with centered differences and by means of a standard linear solutor.

The first equation in (4.45) propagates $\nabla\phi$ isotropically and generates a first approximated vector field $\mathbf{A}_0$. In fig. 4.18 the vector field $\mathbf{A}_0$ related to the Kanizsa inducers is visualized. The second equation generates a better approximation $\mathbf{A}_1$ by propagating $\nabla\phi$ in the direction $\mathbf{A}_0$. In fig. 4.19 the components of the vector field $\mathbf{A}_1$ related to the same inducers is shown. Inducers have been manually selected.

Since particle and field equations are coupled, we can now solve the complete particle equation

$$\phi = \frac{1}{2}\Gamma(x,y) * \Big(\Delta h + \frac{1}{2}(div(\mathbf{A}_1)\Big)$$

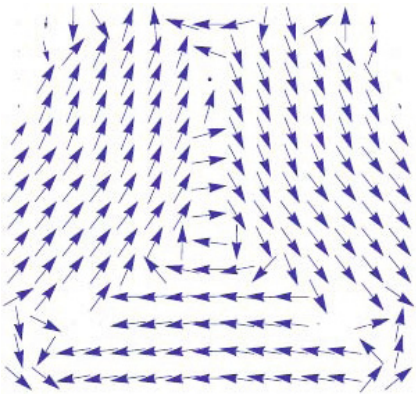

Fig. 4.18 The field $\mathbf{A}_0$ generated by the Kanizsa triangle inducers

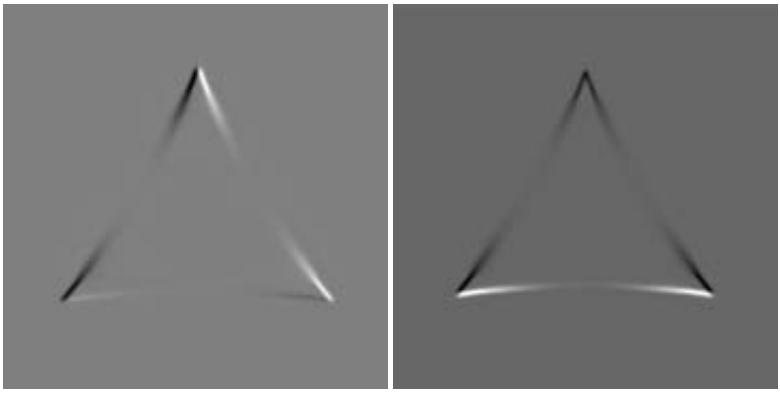

Fig. 4.19 The x and y components of the gauge field $\mathbf{A}_1$ related to the Kanizsa triangle inducers. $\mathbf{A}_1$ is an approximation of the field $\mathbf{A}$, solution of the gauge field equation.

again by convolution with the fundamental solution Γ. This is a version of the Retinex equation able to reconstruct the original image together with the subjective surface. In Fig. 4.20 (left) the forcing term $\frac{1}{2}(\Delta h + div(\mathbf{A}_1))$ of the particle equation is visualized, while in Fig. 4.20 (right) the solution ϕ is shown.

4.7 Stochastic Neurogeometry

The phenomenological experiment conduced by Field, Heyes and Hess [23] shows that the association field allows to perceive configurations of oriented patches preferably fulfilling a co-circularity condition. This result is well modelled by the integral curves of equation (4.20). The experiment shows also that even if the co-circularity

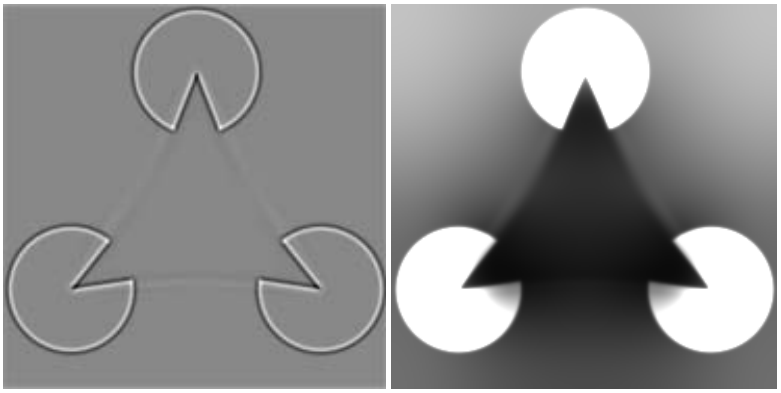

Fig. 4.20 Left: The forcing term $\frac{1}{2}(\Delta h + div(\mathbf{A}_1))$ of the particle equation. Right: The reconstructed Kanizsa triangle as the solution ϕ of the particle equation.

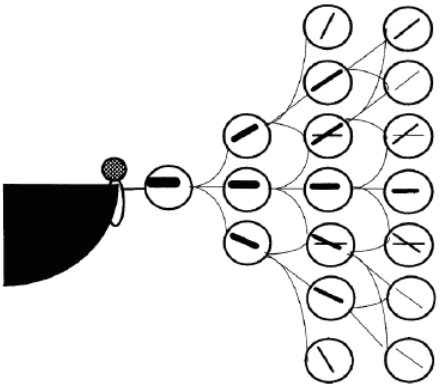

Fig. 4.21 The association field of Field, Heyes and Hess showing that the co-circular configuration of patches is just the most salient among other possible configurations (double bars in a circle).

condition induces a maximum perceptual saliency, all the configurations of patches are perceived with a certain saliency.

To model the saliency of the entire set of perceptual configurations it is necessary to leave the deterministic framework and introduce a stochastic setting that constitutes the probabilistic counter part of the deterministic equation (4.20). David Mumford first introduced a stochastic differential equation in [44] to model partially occluded edges:

$$(x'(t), y'(t), \theta'(t)) = (\cos(\theta(t)), \sin(\theta(t)), N(0, \sigma^2)),$$

where $N(0,\sigma^2)$ is a normally distributed variable with zero mean and variance equal to σ^2. The equation has been further discussed by August-Zucker [1], Williams-Jacobs [59], and Sanguinetti-Citti-Sarti [48] who outlined that it is naturally defined in the SE(2) group structure

$$(x'(t),y'(t),\theta'(t)) = \mathbf{X}_1(\theta(t)) + N(0,\sigma^2)\mathbf{X}_2. \tag{4.46}$$

Indeed both systems (4.20) and (4.46) are represented in terms of left invariant operators of the Lie group, the first one with deterministic curvature, the second with normal random variable curvature. Equation (4.46) describes a random walk with constant speed in a direction randomly changing. Let us denote $p(x,y,\theta,t)$ the probability density to find a particle at the point (x,y) moving with direction $\mathbf{X_1}$ at the instant of time t conditioned by the fact that it started from the point $(x(0)=0,y(0)=0,\theta(0)=0)$. After Ito integration, this probability density satisfies a Kolmogorov Forward Equation or Fokker-Planck equation (FP):

$$\begin{aligned}\partial_t p(x,y,\theta,t) &= X_1 p(x,y,\theta,t) + \sigma^2 X_{22} p(x,y,\theta,t) \\ &= \cos(\theta)\partial_x p(x,y,\theta,t) + \sin(\theta)\partial_y p(x,y,\theta,t) + \sigma^2 \partial_{\theta\theta} p(x,y,\theta,t).\end{aligned} \tag{4.47}$$

Let us notice that the equation (4.47) consists of an advection term in the direction $\mathbf{X}_1$ and a diffusion term in the direction $\mathbf{X}_2$, where the doubling of the index expresses a second order derivation.

This equation has been largely used in computer vision and applied to perceptual completion related problems. It was used by Williams and Jacobs in [59] to compute stochastic completion field, by S. Zucker and his collaborators in [1] to define the curve indicator random field, and more recently by R. Duits et Al. in [25] applying it to perform contour completion, denoising and contour enhancement. In [48] it was proposed to consider the stationary counterpart of (4.47) to model both the Fields, Heyes and Hess association field and the probability of co-occurence of contours in natural images. Both the phenomenon are indeed stationary.

For this purpose, we integrate eq. (4.47) in time, obtaining the stationary equation

$$X_1 p(x,y,\theta) + \sigma^2 X_{22} p(x,y,\theta) = \delta(x,y,\theta). \tag{4.48}$$

Equation (4.48) is strongly biased in direction $\mathbf{X}_1$, and to take into account the symmetry of both association fields and edge cooccurences, the model for the probability density propagation has been symmetrized considering the backward FP equation in the opposite direction

$$-X_1 p(x,y,\theta) + \sigma^2 X_{22} p(x,y,\theta) = \delta(x,y,\theta). \tag{4.49}$$

The desired fundamental solution is then obtained by summing the Green functions corresponding to forward and backward FP equations.

The fundamental solution has been computed numerically with standard Markov Chain Monte Carlo methods. This is done by generating random paths obtained from numerical solutions of the stochastic system and averaging their passages over

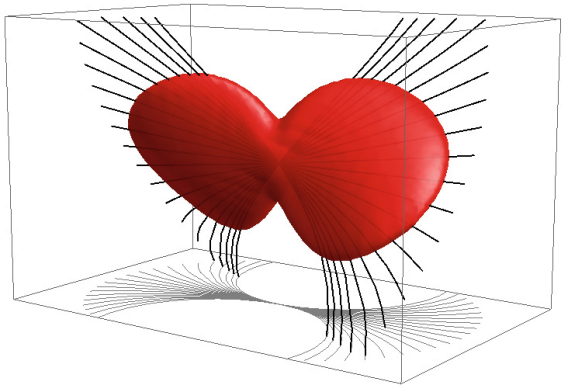

Fig. 4.22 The sum of fundamental solutions of the stationary Fokker Planck equations (4.48) and (4.49). An isosurface of intensity is visualized in red together with the integral curves of the group eq. (4.20).

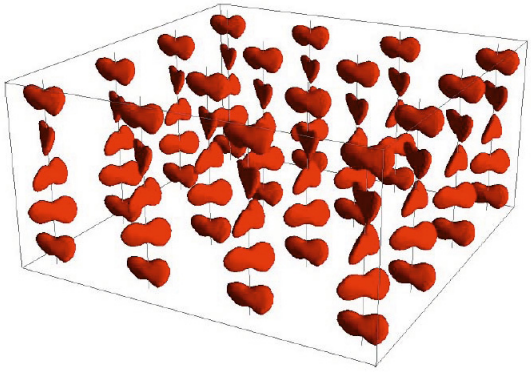

Fig. 4.23 The stochastic neurogeometry as fundamental solution of stationary Fokker Planck equation. It is a "fat" version of the deterministic structure visualized in Fig. 4.7

discrete volume elements. See [40] for a classical and complete description of the technique. In Fig.4.22 the sum of fundamental solutions of the stationary Fokker Planck equations (4.48) and (4.49) is visualized together with the integral curves of the group eq. (4.20). Note that the kernel seems to be a thick version of the fan (4.20). The value of the probability decays slowly along the integral curves and quickly in the direction normal to the surface ruled by the integral curves. In Fig. 4.23 the entire set of fundamental solutions is visualized in the space (x, y, θ). Notice that it is a "fat" version of the deterministic structure visualized in Fig.4.7.

4.7.1 The Statistics of Edges in Natural Images

It can be of some interest to question the origin of the very specific shape of the association field in its deterministic or stochastic version. An intriguing hypothesis is that association fields have been learned by the visual stimuli and then that the particular pattern comes from some statistical property of natural images.

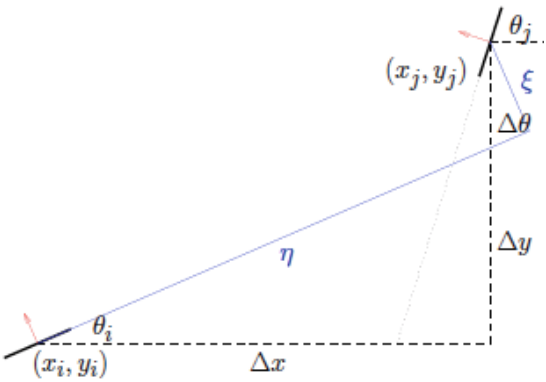

Fig. 4.24 Geometric schemata of co-occurences of edges: a co-occurrence takes place when two edges (x_i, y_i, θ_i) and (x_j, y_j, θ_j) occur at the same time in the image. Only relative positions $(\Delta x, \Delta y)$ and orientations $\Delta\theta$ are taken into account in the computation of histograms.

A specific study to assess the existence of this relation has been proposed in [48]. Research has been focused on the statistics of edges in natural images and particularly in the statistics of co-occurrence of couples of edges taking into account its relative position and orientation. The statistics have been estimated analyzing a number of natural images from which a multidimensional histogram of relative position and orientation of edges has been constructed. Images have been preprocessed by linear filtering with a set of oriented edge detection kernels (Gabor filters) and performing non maximal suppression. A list of pixels corresponding to edges with their respective orientations has been obtained by thresholding and binarization. A four dimensional histogram $(\Delta x, \Delta y, \theta_c, \theta_p)$ has been computed by counting how many times two detected edges with relative positions $(\Delta x, \Delta y)$ have orientations (θ_c, θ_p). Finally a 3D histogram $(\Delta x, \Delta y, \Delta\theta)$ is obtained where the third coordinate is the relative orientation $\Delta\theta = \theta_p - \theta_c$.

4.7.2 Comparison between the Statistics of Edges and the Stochastic Structure

A comparison between the estimated statistical distribution of edges and the computed stochastic neurogeometrical model has been performed in [48]. In Fig. 4.27

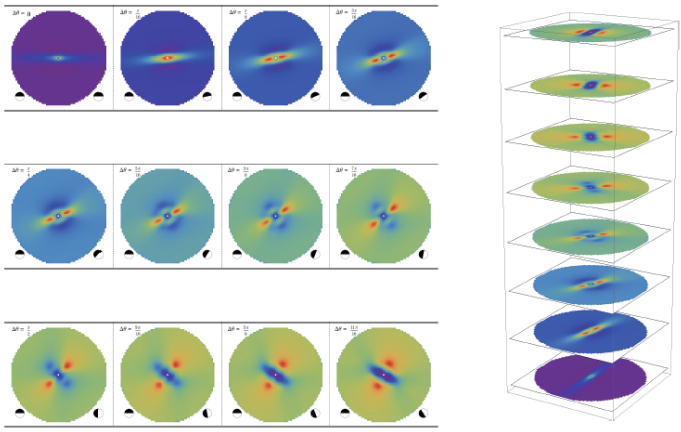

Fig. 4.25 Sections of the co-occurence maps $(\Delta x, \Delta y)$ for different pairs of orientations $\Delta\theta$ (left). Sections are piled up to build the 3D distributions $(\Delta x, \Delta y, \Delta\theta)$ (right).

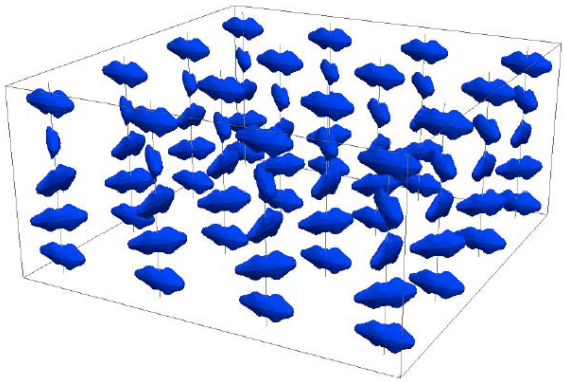

Fig. 4.26 The whole distribution of co-occurrence of edges in natural images in the space (x, y, θ). It can be interesting compare this distribution with the deterministic structure visualized in Fig. 4.7 and the stochastic structure of Fig. 4.23.

the two distributions are visualized and compared. There are two degrees of freedom in the model to match: the variance σ of the Fokker Plank operator and a scale factor. After performing the parameter identification, the relative difference between both functions is less than 0.02, and the reported value for σ is 1.71, a very interesting value since it estimates the variance of the co-occurrence random process.

We found that it is possible to recover the co-circularity pattern from both the distributions with the following procedure. First we compute the surface of maximal probability $\bar{\theta}(x, y)$, where

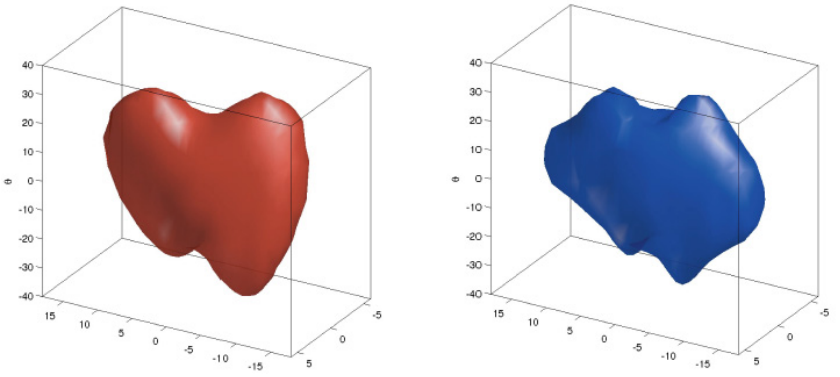

Fig. 4.27 Comparison between the computed stochastic model (left) and the distribution of edge cooccurrences in natural images (right). The percentual error between the two distributions is less than 2.

$$\max_{\theta} p(x,y,\theta) = p(x,y,\bar{\theta}).$$

Secondly, the integral curves of the vector field $(\cos\bar{\theta}(x,y), \sin\bar{\theta}(x,y))$ are computed. We found that in both cases curves present co-circularity. See Fig. 4.28 for a comparison. These comparisons strongly suggest that horizontal connectivity modeled by the neurogeometry is deeply shaped by the statistical distributions of features in the environment and that the very origin of neurogeometry as to be discovered in the interaction between the embodied subject and the world.

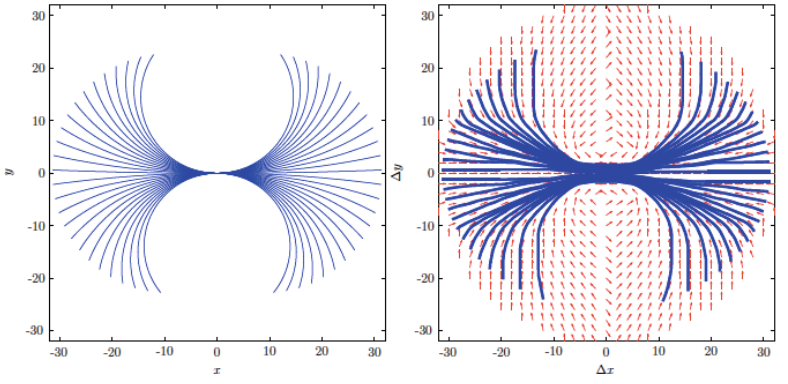

Fig. 4.28 The co-circularity constraint in the neurogeometrical model, as the projection of integral curves (left), and in the statistics of natural images as integral curves of the projected vector field (right)

4.8 A Harmonic Neurogeometrical Model

4.8.1 The Binding Problem and the Constitution of Perceptual Units

The question of constitution of perceptual units is central in the entire body of study of visual organization. The issue deals with the mechanism allowing the information distributed in the visual areas to get bound together into coherent object representations. Electromagnetic radiations (photons) going from the physical world to the eye are completely independent one to the other and do not contain any explicit information about the unitarity of objects. The visual areas are constituted in its turn by million of cells. Along this path the unity of physical objects is completely lost, but at the end of the chain the object shows up again at the perceptual level as a unit. In which way is this reconstruction possible?

This process is known as "binding" or "perceptual grouping", and it has been extensively studied both from a phenomenological point of view by the experimental psychology of Gestalt [34] and from a neuro-physiological point of view aiming to clarify its biological functionalities. Even if the mechanism of grouping is still unknown there is a wide experimental evidence that the constitution of a perceptual unit involves the response of a large number of neurons distributed over a large spatial region. Different answers have been proposed to explain how these distributed neural activities are integrated together to constitute a unit.

If excitatory-inhibitory neural populations are considered, the most accreditated hypothesis is that binding is implemented with a temporal coding, meaning that object segmentation is performed by the synchronization of oscillatory neural responses [28]. Many models have been proposed to explain phase locking of populations of neural oscillators, see for example [56] for a review. In [11, 51] it has been shown that a neurophysiological model of coupled neural oscillators in phase locking tends in its continuous spatial limit to the phenomenological model of segmentation of Mumford-Shah.

On the other hand, if single population models are considered, different mechanisms for binding can arise. For example in [52] and [53] a mechanism of grouping has been proposed as an extension of the model of visual hallucination proposed by Bressloff and Cowan [7]. We will reconsider extensively this model in the following. Particularly we want to investigate what is the role of the neurogeometry in the constitution of perceptual units, considering that a global integration process is needed. As stated by the studies of Gestalt theory, perception is a global process. Moreover visual perception acts as a differentiation process of the entire field of view, performing first a differentiation between figure and ground, and continuing in the segmentation of single objects. We will try to keep in mind these fundamental points and to formalize them in a coherent model.

4.8.2 The Population Model

As shown in [53], the Ermentraut-Cowan mean field population model in presence of a cortical input stimulus $h(x,y,\theta)$ provided by simple cells is

$$\frac{\mathrm{d}a(x,y,\theta,t)}{\mathrm{d}t} = -\alpha a(x,y,\theta,t) + \sigma_\gamma\Big(\omega * a(x,y,\theta,t) + \frac{h(x,y,\theta)}{\alpha}\Big) \tag{4.50}$$

where $a(x,y,\theta,t)$ is the neural activity of the population and α is the decay constant.

The kernel $\omega\Big((x,y,\theta),(x',y',\theta')\Big)$ is the weight of connectivity between the population at the position (x,y) tuned at the orientation θ and the one at the position (x',y') tuned at θ', and it can be modelled by the fundamental solution of the stationary Fokker-Planck equation (4.48). It takes into account the contribution of cortico-cortical connectivity.

The function σ_γ is the transfer function of the population and it has the classical sigmoidal behavior:

$$\sigma_\gamma(\xi) = \frac{1}{1+e^{-\gamma(\xi-\chi)}} - 1/2,$$

where χ is the threshold and γ is the gain. Notice that $\sigma(\chi) = 0$ and this happens when the input term $h = \alpha\chi$. For simplicity we will consider here a piecewise constant input $h = \alpha\chi$ in a domain $\Omega : \{(x,y,\theta) : h(x,y,\theta) = \alpha\chi\}$ and $h = 0$ elsewhere. Note that in case of weak connectivity kernel, neurons outside Ω will stay constant and under threshold in the dynamic of the system.

Then the activity equation becomes

$$\frac{\mathrm{d}a(x,y,\theta,t)}{\mathrm{d}t} = -\alpha a(x,y,\theta,t) + \tilde{\sigma}_\gamma(\omega * a(x,y,\theta,t)) \tag{4.51}$$

for $(x,y,\theta) \in \Omega$, where

$$\tilde{\sigma}_\gamma(\xi) = \sigma_\gamma(\xi - h/\alpha)$$

with the property $\tilde{\sigma}_\gamma(0) = 0$. Let us outline that eq. (4.51) is formally equivalent to the population equation studied by Bressloff and Cowan in [7] but defined in a domain Ω instead of in the entire $\mathbb{R}^2$. We will study it with the same instruments here.

4.8.3 Solutions of the Activity Equation

To compute stationary states of the activity equation (4.51), it is trivial to check that since $\tilde{\sigma}_\gamma(0) = 0$ then the homogeneous state $a(x,y,\theta,t) = 0$ on the domain Ω is a stationary solution.

The stability of the solution can be studied in terms of eigenvalues of the linearized functional

$$La = -\alpha a + \gamma\omega * a$$

in the domain Ω where $\gamma = \sigma'(0)$. Eigenvalues λ verify the equation

$$\lambda a = -\alpha a + \gamma \omega * a,$$

that is equivalent to the eigenvalue problem

$$\tilde{\lambda} a = \omega * a$$

provided that $\tilde{\lambda} = \frac{(\alpha+\lambda)}{\gamma}$. Then the stability problem is reduced to the study of eigenvectors of the connectivity kernel ω in the domain Ω, meaning the operator $K(a) = \omega * a$ in Ω. Since ω is the fundamental solution of the stationary Fokker Planck equation (4.48), the convolution operator $K(a)$ is compact, and its largest positive eigenvalue is real. Moreover it has infinitely many eigenvalues, and the sequence of eigenvalues tends to 0.

This means that, when γ is small, zero is a stable solution, and it remains stable until $\frac{\alpha a_0}{\gamma}$ takes the value of the largest eigenvalue of $K(a)$. While γ further increases, the solution remains unstable.

(The eigenvectors of the operator K become marginally stable. Also note that the corresponding eigen-space is of finite dimension since the operator K is compact.)

4.8.4 The Discrete Case

If the activity $a(x,y,\theta)$ is approximated by a discrete distribution in terms of Dirac masses

$$a = \sum_{i=1}^{h} a_i \delta_{(x_i,y_i,\theta_i)},$$

then the convolution operator becomes

$$\omega * a = \sum_{j=1}^{n} \omega((x_i,y_i,\theta_i)(x_j,y_j,\theta_j))a_j = \tilde{\lambda} a_i.$$

Note that in this case the eigenvalue problem on the activity $a(x,y,\theta)$ reduces to the spectral analysis of the matrix

$$A_{ij} = \omega((x_i,y_i,\theta_i)(x_j,y_j,\theta_j))$$

with usual linear agebra instruments.

This matrix can be considered as the equivalent of the *affinity matrix* introduced by Perona in [45] to perform perceptual grouping.

Perona proposed to model the affinity matrix in term of a euristic distance $d(x,y,\theta)$, facilitating collinear and cocircular couple of elements

$$A_{ij} = e^{-d^2((x_i,y_i,\theta_i)(x_j,y_j,\theta_j))}.$$

In our case it is possible to prove that the distance d corresponds to the formal Carnot Carathéodory distance d_c, meaning the geometric sub-Riemannian distance

induced by the horizontal connectivity, since the fundamental solution ω can be approximated by:

$$\omega((x_i, y_i, \theta_i), (x_j, y_j, \theta_j)) \simeq e^{-d_c{}^2((x_i,y_i,\theta_i),(x_j,y_j,\theta_j))}.$$

See [6] for a formal proof.

4.8.5 Dimensionality Reduction

In [45] the problem of perceptual grouping has been faced in terms of reduction of the complexity in the description of a scene. The visual scene is described in terms of the affinity matrix A_{ij} with a complexity of order $O(N^2)$ if N discrete elements are present in the scene. The idea of Perona is to describe the scene by a point-wise function p_i of objects i taken one by one, rather than by a function A_{ij} of object pairs (i, j). This way the complexity of the description will drop to O(N). A way to reduce by one order of magnitude the complexity of the description is to consider the best approximation of the affinity matrix

$$p = argmin_{\hat{p}} \sum_{i,j=1}^{N} (A_{i,j} - \hat{p}_i \hat{p}_j)^2$$

where the term $\mathbf{pp}^T$ is a rank one matrix with complexity order $O(N)$.

Perona proved that the minimizer p of the Frobenius norm is the first eigenvector v_1 of the matrix A with largest eigenvalue λ: $p = \lambda_1^{1/2} v_1$.

Then the problem of grouping is reduced to the spectral analysis of the affinity matrix $A_{i,i}$, where the salient objects in the scene correspond to the first eigenvectors with largest eigenvalues. We just showed in the previous paragraphs that this eigenvalue analysis can be accomplished by the activity of neural populations connected by means of cortico-cortical horizontal connectivity.

4.8.6 Constitution of Perceptual Units

The affinity matrix can be represented as a graph whose nodes are the active cells and the links are the neural connectivities with a weight that is defined in terms of the connectivity kernel $\omega((x_i, y_i, \theta_i)(x_j, y_j, \theta_j))$ (see Fig. 4.29).

Figure-ground articulation and the segmentation of different objects will correspond to different eigenvectors a_i. In Fig. 4.30 the three principle eigenvectors of the neurogeometrical matrix associated to Fig. 4.29 are visualized in gray values, showing the global emergence of perceptual units.

Let us note that this approach interprets the emergent figures in the image as eigenstates of the neurogeometrical matrix A_{ij}. Mathematically it corresponds to the singular value decomposition of the neurogeometrical graph previously defined. Co-occurring features are mapped to the same eigenvector; features that do not co-occur are mapped to different eigenvectors. The eigenvector linked to the highest

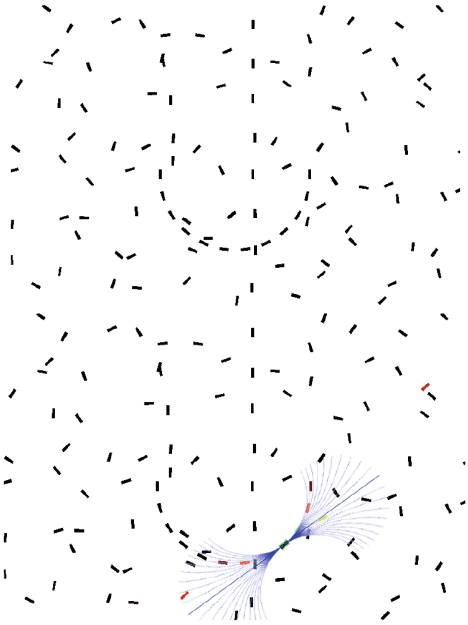

Fig. 4.29 Some perceptual units are perceived as coherent structures out of a random distribution of segments. In the image on the top the most salient features are the semicircle and a vertical segment. Neurogeometry lifts every segment in the E(2) group and induces connectivity weights between every couple of segments represented in colors (bottom). The affinity matrix A_{ij} is constructed with the corresponding weights between couples of segments $i - j$.

singular value represents the most important vector in the data (i.e. the vector that explains the most variance of the matrix); the singular vectors linked to the second highest value represent the second most important vector (orthogonal to the first one), and so on.

Models of image segmentation based on singular value decomposition and in general on dimensionality reduction are largely used in contemporary computer vision (see for example [45], [54]), and we refer to [58] for a review of methods. We have shown in this chapter how these sophisticated models of image segmentation can be implemented at a neural level in terms of harmonic analysis of the neurogeometry.

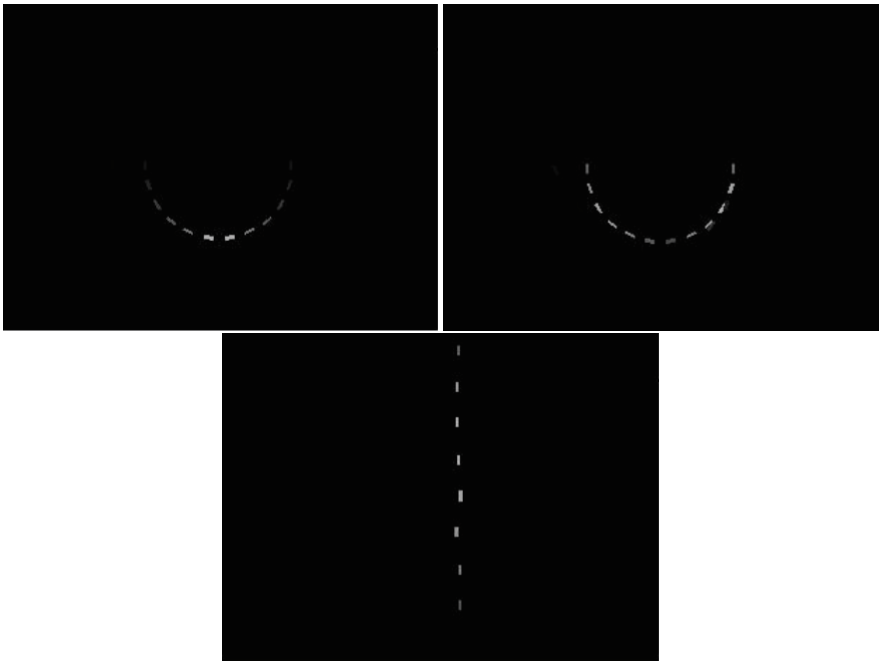

Fig. 4.30 Eigenvectors of the affinity matrix are visualized mapping the intensity in gray levels. The first a_i eigenvectors correspond to the most salient perceptual units.

Acknowledgement. The authors are grateful to Giacomo Cocci and Gonzalo Sanguinetti, who realized some of the figures present in the text and to Davide Barbieri for his patience and dedication in the formatting of the book.

References

1. August, J., Zucker, S.W.: Sketches with curvature: The curve indicator random field and markov processes. IEEE Transactions on Pattern Analysis and Machine Intelligence 25(4), 387–400 (2003)
2. Barbieri, D., Citti, G., Sanguinetti, G., Sarti, A.: An uncertainty principle underlying the functional architecture of V1. Journal of Physiology Paris 106(5-6), 183–193 (2012)
3. Barbieri, D., Citti, G.: Reproducing kernel Hilbert spaces of CR functions for the Euclidean Motion group (submitted)
4. Bargmann, V.: On a Hilbert space of analytic functions and an associated integral transform. Part II. Application to distribution theory. Comm. Pure Appl. Math. 20, 1–101 (1967)
5. Barles, G., Georgelin, C.: A simple proof of convergence for an approximation scheme for computing motions by mean curvature. SIAM Journal on Numerical Analysis 32(2), 484–500 (1995)
6. Bonfiglioli, A., Uguzzoni, F., Lanconelli, E.:

7. Bressloff, P.C., Cowan, J.D.: The functional geometry of local and long-range connections in a model of V1. J. Physiol. Paris 97(2-3), 221–236 (2003)
8. Bressloff, P.C., Cowan, J.D., Golubitsky, M., Thomas, P.J., Wiener, M.: Geometric visual hallucinations, Euclidean symmetry and the functional architecture of striate cortex Phil. Trans. Roy. Soc., B 40, 299–330 (2001)
9. Carruthers, P., Nieto, M.M.: Phase and Angle Variables in Quantum Mechanics. Reviews of Modern Physics 40(2), 411–440 (1968)
10. Capogna, L., Citti, G., Senni, C., Magnani, G.: Sub-Riemannian heat kernel and mean curvature flow of graphsJFA (2013)
11. Citti, G., Manfredini, M., Sarti, A.: Neuronal Oscillations in the Visual Cortex: Gamma-convergence to the Riemannian Mumford-Shah Functional. SIAM Journal Mathematical Analysis 35(6), 1394–1419 (2004)
12. Citti, G., Sarti, A.: A cortical based model of perceptual completion in the Roto-Translation space. Journal of Mathematical Imaging and Vision 24(3), 307–326 (2006)
13. Citti, G., Sarti, A.: A cortical based model of perceptual completion in the Roto-Translation space. Journal of Mathematical Imaging and Vision 24(3), 307–326 (2006)
14. Citti, G., Sarti, A.: A Gauge Field model of modal completion (submitted)
15. Cohen-Tannoudji, C., Dui, B., Laloe, F.: Quantum Mechanics. John Wiley & Sons (1978)
16. Crair, M., Ruthazer, E., Gillespie, D., Stryker, M.: Ocular Dominance Peaks at Pinwheel Center Singularities of the Orientation Map in Cat Visual Cortex. J. Neurophysiol. 77(6), 3381–3385 (1997)
17. Daugman, J.G.: Uncertainty-relation for resolution in space, spatial frequency and orientation optimized by two dimensional visual cortical filters. J. Opt. Soc. Amer. 2(7), 1160–1169 (1985)
18. De Angelis, G.C., Ozhawa, I., Freeman, R.D.: Receptive-field dynamics in the central visual pathways. Trends Neurosci. 18(10), 451–458 (1995)
19. Duits, R., Franken, E.M.: Left invariant parabolic evolution equations on SE(2) and contour enhancement via invertible orientation scores, part I: Linear left-invariant diffusion equations on SE(2). Q. Appl. Math. 68, 255–292 (2010)
20. Duits, R., Franken, E.M.: Left invariant parabolic evolution equations on SE(2) and contour enhancement via invertible orientation scores, part II: Nonlinear left-invariant diffusion equations on invertible orientation scores. Q. Appl. Math. 68, 293–331 (2010)
21. Duits, R., Führ, H., Janssen, B., Bruurmijn, M., Florack, L., Van Assen, H.: Evolution equations on Gabor transforms and their applications. arXiv:1110.6087 (2011)
22. Evans, L.C.: Convergence of an algorithm for mean curvature motion. Indiana Univ. Math. J. 42(2), 533–557 (1993)
23. Field, D.J., Hayes, A., Hess, R.F.: Contour integration by the human visual system: evidence for a local Association Field. Vision Research 33, 173–193 (1993)
24. Folland, G.: Harmonic analysis on phase space. Princeton University Press (1989)
25. Franken, E., Duits, R., ter Haar Romeny, B.M.: Nonlinear Diffusion on the 2D Euclidean Motion Group. In: Sgallari, F., Murli, A., Paragios, N. (eds.) SSVM 2007. LNCS, vol. 4485, pp. 461–472. Springer, Heidelberg (2007)
26. Georgiev, T.: Covariant derivatives and vision. In: Leonardis, A., Bischof, H., Pinz, A. (eds.) ECCV 2006. LNCS, vol. 3954, pp. 56–69. Springer, Heidelberg (2006)
27. Georgiev, T.: Vision, healing brush, and fibre bundles. In: Proceedings of SPIE - The International Society for Optical Engineering, vol. 5666, p. 33, pp. 293–305 (2005)
28. Gray, C.M., König, P., Engel, A.K., Singer, W.: Oscillatory responses in cat visual cortex exhibit inter-columnar synchronization which reflects global stimulus properties. Nature 338, 334–337 (1989)

29. Hladky, R., Pauls, S.: Minimal Surfaces in the Roto-Translation Group with Applications to a Neuro-Biological Image Completion Model. Journal of Mathematical Image and Vision 36, 1–27 (2010)
30. Hoffman, W.C.: The visual cortex is a contact bundle. Applied Mathematics and Computation 32, 137–167 (1989)
31. Horn, B.K.P.: Determining lightness from an image. Comput. Graph. Image Process., 277–299 (1974)
32. Hubel, D.H.: Eye, Brain and Vision. Scientific American Library, New York (1988)
33. Hubel, D.H., Wiesel, T.N.: Ferrier lecture: Functional architecture of macaque monkey visual cortex. Proceedings of the Royal Society of London Series B 198(1130), 1–59 (1977)
34. Kanizsa, G.: Grammatica del vedere. Il Mulino, Bologna (1980)
35. Kimmell, R., Elad, M., Shaked, D., Keshet, R., Sobel, I.: A Variational Framework for Retinex. International Journal of Computer Vision 52(1), 7–23 (2003)
36. Lee, T.S.: Image Representation Using 2D Gabor Wavelets. IEEE Transection of Pattern Analysis and Machine Intelligence 18(10), 959–971 (1996)
37. Land, E.H.: The Retinex theory of color vision. Scientific American 237(6), 108–128 (1977)
38. Land, E., McCann, J.: Lightness and Retinex theory. J. Opt. Soc. Amer. 61(1), 1–11 (1971)
39. Marr, D.: Vision. Freeman (1982)
40. Robert, C.P., Casella, G.: Monte Carlo statistical methods, 2nd edn. Springer (2004)
41. Niebur, E., Wörgötter, F.: Design Principles of Columnar Organization in Visual Cortex. Neural Computation 4(6), 602–614 (1994)
42. Merriman, B., Bence, J., Osher, S.J.: Diffusion generated motion by mean curvature. In: Taylor, J. (ed.) Proceedings of the Computational Crystal Growers Workshop, pp. 73–83. AMS, Providence (1992)
43. Morel, J.-M.: A PDE Formalization of Retinex Theory. IEEE Transactions on Image Processing 19(11) (2010)
44. Mumford, D.: Elastica and computer vision. In: Algebraic Geometry and its Applications, West Lafayette, IN, pp. 491–506. Springer, New York (1990, 1994)
45. Perona, P., Freeman, W.T.: A factorization approach to grouping. In: Burkhardt, H.-J., Neumann, B. (eds.) ECCV 1998. LNCS, vol. 1406, pp. 655–670. Springer, Heidelberg (1998)
46. Petitot, J., Tondut, Y.: Tondut, Vers une Neurogeometrie. Fibrations corticales, structures de contact et contours subjectifs modaux, Mathematiques. Informatique et Sciences Humaines, vol. 145, pp. 5–101. EHESS, CAMS, Paris (1999)
47. Petitot, J., Varela, F., Pachoud, B., Roy, J.-M.: Naturalizing Phenomenology: Issues in Contemporary Phenomenology and Cognitive Science. Stanford University Press (1999)
48. Sanguinetti, G., Citti, G., Sarti, A.: A Stochastic Model for Edges in Natural Images using Lie Groups. To appear in Journal of Vision (2010)
49. Sarti, A., Citti, G., Petitot, J.: The Symplectic Structure of the Primary Visual Cortex. Biol. Cybern. 98, 33–48 (2008)
50. Sarti, A., Citti, G., Petitot, J.: Functional geometry of the horizontal connectivity in the primary visual cortex. Journal of Physiology-Paris 103(1-2), 37–45 (2009)
51. Sarti, A., Citti, G., Manfredini, M.: From Neural Oscillations to Variational Problems in the Visual Cortex. Journal of Physiology Paris 97(2-3), 379–385 (2003)
52. Sarti, A., Citti, G.: On the origin and nature of neurogeometry. La Nuova Critica (2011)
53. Sarti, A., Citti, G.: Visual perceptual units as constrained hallucinations (submitted)

54. Shi, J., Malik, J.: Normalized cuts and image segmentation. In: Proc. IEEE Conf. Comp. Vis. Pat. Rec., pp. 731–737 (1997)
55. Sugiura, M.: Unitary representations and harmonic analysis, an introduction. Elsevier (1990)
56. Wang, D.: Emergent synchrony in locally coupled neural oscillators. IEEE Trans. Neural Networks 6, 941–948 (1995)
57. Webb, B., Tinsley, C.J., Vincent, C.J., Derrington, A.M.: Spatial Distribution of Suppressive Signals Outside the Classical Receptive Field in Lateral Geniculate Nucleus. J. Neurophysiol. 94, 1789–1797 (2005)
58. Weiss, Y.: Segmentation using eigenvectors: a unifying view. In: Proc. IEEE Int. Conf. on Comp. Vis., pp. 975–982 (1999)
59. Williams, L.R., Jacobs, D.W.: Local Parallel Computation of Stochastic Completion Fields. Neural Comp. 9(4), 859–881 (1997)
60. Wilson, H.R., Cowan, J.D.: Excitatory and inhibitory interactions in localized populations of model neurons. Biophys. J. 12, 1–24 (1972)
61. Zucker, S.W.: Differential geometry from the Frenet point of view: boundary detection, stereo, texture and color. In: Paragios, N., Chen, Y., Faugeras, O. (eds.) Handbook of Mathematical Models in Computer Vision, pp. 357–373. Springer, US (2006)